

Topologically non-trivial valley states in bilayer graphene quantum point contacts

Hiske Overweg,^{1,*} Angelika Knothe,² Thomas Fabian,³ Lukas Linhart,³ Peter Rickhaus,¹
Lucien Wernli,¹ Kenji Watanabe,⁴ Takashi Taniguchi,⁴ David Sánchez,⁵ Joachim
Burgdörfer,³ Florian Libisch,³ Vladimir I. Fal'ko,² Klaus Ensslin,¹ and Thomas Ihn¹

¹*Solid State Physics Laboratory, ETH Zürich, CH-8093 Zürich, Switzerland*

²*National Graphene Institute, University of Manchester, Manchester M13 9PL, UK*

³*Institute for Theoretical Physics, Vienna University of Technology, A-1040 Vienna, Austria*

⁴*National Institute for Material Science, 1-1 Namiki, Tsukuba 305-0044, Japan*

⁵*Institute for Cross-Disciplinary Physics and Complex Systems IFISC (UIB-CSIC), 07122 Palma de Mallorca, Spain*

(Dated: September 7, 2018)

We present measurements of quantized conductance in electrostatically induced quantum point contacts in bilayer graphene. The application of a perpendicular magnetic field leads to an intricate pattern of lifted and restored degeneracies with increasing field: at zero magnetic field the degeneracy of quantized one-dimensional subbands is four, because of a twofold spin and a twofold valley degeneracy. By switching on the magnetic field, the valley degeneracy is lifted. Due to the Berry curvature states from different valleys split linearly in magnetic field. In the quantum Hall regime fourfold degenerate conductance plateaus reemerge. During the adiabatic transition to the quantum Hall regime, levels from one valley shift by two in quantum number with respect to the other valley, forming an interweaving pattern that can be reproduced by numerical calculations.

Conductance quantization in one-dimensional channels is among the cornerstones of mesoscopic quantum devices. It has been observed in a large variety of material systems, such as n -type GaAs [1, 2], p -type GaAs [3, 4], SiGe [5], GaN [6], InSb [7], AlAs [8] and Ge [9]. Typically spin degeneracy leads to quantization in multiples of $2 e^2/h$. In single and bilayer graphene both steps of $2 e^2/h$ and $4 e^2/h$ have been reported [10–15], although a fourfold degeneracy is expected due to the additional valley degree of freedom. Here we present data for three quantum point contacts (QPCs) which display (approximately) fourfold degenerate modes both at zero magnetic field and in the quantum Hall regime, and twofold degenerate modes in the transition region. The Berry curvature in gapped bilayer graphene induces an orbital magnetic moment for the states selected by the quantum point contact. The valleys therefore split linearly in a weak magnetic field and conductance steps of $2e^2/h$ emerge. The adiabatic evolution of conduction steps to the quantum Hall regime reveals a universal level crossing pattern: state energies in one valley shift by two with respect to those of the other valley due to the chirality of the effective low-energy Hamiltonian in the K_+ and K_- valley, a general feature of Dirac particles in even spatial dimensions [16]. Related topological effects involving the valley degree of freedom have recently been discussed in bilayer [17–20] and trilayer graphene [21]. The lifting and restoring of level degeneracies is explained in detail by two complementary theoretical models. These results are the basis for a detailed understanding of conductance quantization and tunneling barriers in bilayer graphene, enabling high-quality quantum devices.

The device geometry is similar to the one employed in our demonstration of full pinch-off of bilayer graphene

quantum point contacts [15]. A bilayer graphene (BLG) flake was encapsulated between hexagonal boron nitride layers (hBN), using the van der Waals pick-up technique [22], and deposited onto a graphite flake (see Figure 1a for a schematic of the final device geometry). The graphene layer was contacted with Cr/Au contacts and a top gate pattern, consisting of six pairs of split gates (SG) with spacings ranging from 50 nm to 180 nm, was evaporated. On top of the device a layer of Al_2O_3 and finally the channel gates (CH) were deposited. An atomic force microscopy image of the sample, recorded prior to the deposition of the channel gates, is shown in Fig. 1b. In the present manuscript, we show data from three QPCs: QPC S (50 nm split gate separation), QPC M (80 nm) and QPC L (180 nm).

By applying voltages of opposite sign to the graphite back gate and the split gates, a band gap is induced [23] in the bilayer graphene. In Ref. 15 we demonstrated that this suppresses transport below the split gates. Hence a constriction is formed, in which the charge carrier density can be tuned by the channel gate voltage. During the measurements only a single pair of split gates was biased at a time to form a QPC. The measurements were performed at $T = 1.7$ K.

The conductance of QPC M (80 nm wide) as a function of channel gate voltage is shown in Fig. 1c for various combinations of the split and back gate voltage. For each curve, a series resistance was subtracted which corresponds to the resistance measured at the same back gate voltage with uniform charge carrier density throughout the sample. The traces show several plateaus with a typical step size of $\Delta G = 4 e^2/h$, in particular for large quantum numbers, as previously reported in Ref. 15. Similar results have been found for QPC L and L' (180 nm wide) with a smaller spacing in gate voltage between the plateaus, in agreement with the wider channel, and for QPC S (50 nm wide) with a larger spacing.

* overwegh@phys.ethz.ch

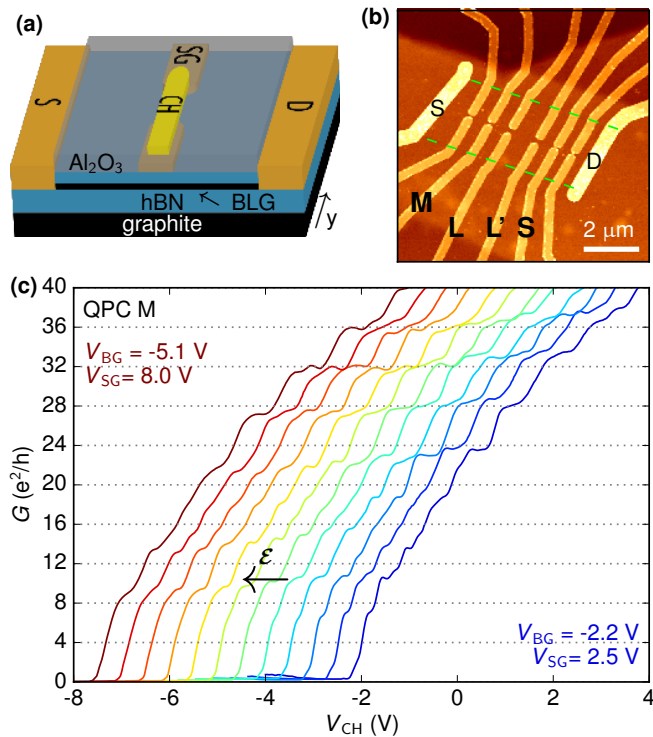


FIG. 1. (a) Schematic of the device consisting of bilayer graphene encapsulated in hBN on top of a graphite back gate. On top of the device split gates were evaporated. A layer of Al_2O_3 serves to separate the split gates from the channel gate. (b) Atomic force microscopy image of the device. Green dashed lines denote the edges of the bilayer graphene flake. Contacts are labeled S and D. Six pairs of split gates are situated between the contacts. (c) Conductance as a function of channel gate voltage for various combinations of the split gate and back gate voltage, showing conductance plateaus with a step size of $\Delta G = 4e^2/h$ for large quantum numbers.

For the employed range of gate voltages, the displacement field \mathcal{E} does not significantly change the observed plateau sequence. Below $G = 24 e^2/h$ we observe several kinks which cannot be identified as plateaus and some plateaus occurring below the expected conductance values. Reduced screening of the disorder potential in this low density regime might play a role. Simulations of the electrostatic potential [15] show that in this regime the confinement potential is shallow. From a theoretical perspective the non-monotonicity of the dispersion relation, which becomes more pronounced for larger gaps and wider channels, can lead to additional degeneracies for low mode numbers, possibly explaining the absence of a plateau at $G = 4 e^2/h$ [24].

The conductance of QPC M as a function of channel gate voltage for several magnetic field strengths (Figure 2a) features a plateau sequence at $B = 0$ T described by $G = 4Ne^2/h$ with integer N . Increasing the magnetic field to a value of $B = 2.2$ T changes the plateau sequence to $G = 2Ne^2/h$. At $B = 5$ T the conven-

tional sequence of Landau levels of BLG is observed, with $G = 4Ne^2/h$. In the lowest two Landau levels a lifting of the fourfold degeneracy can be observed. Around $B = 1.5$ T, during the transition to the Hall regime, the fourfold degeneracy is restored: the sequence is shifted to $G = (4N + 2)e^2/h$. This is most clearly visible for the modes for which $G \geq 22 e^2/h$.

To further investigate this transition we inspect the transconductance as a function of channel gate voltage and magnetic field (see Fig. 2b). Mode transitions show up as dark lines, which start out vertically in low magnetic fields, but bend toward more positive gate voltages above $B = 1$ T. This phenomenon, known as magnetic depopulation and observed for instance in high quality GaAs, is due to the transition from electrostatic confinement to magnetic confinement. What is unusual however, is the pattern of mode splittings and mode crossings.

The same pattern can be observed for the wider QPCs (Fig. 2c), where the fourfold degeneracy is already restored at 2 T because of the wider channel. Although the lowest modes are hard to resolve, a robust pattern of mode crossings can be observed for many higher modes. Similar patterns could be observed for various displacement fields inside the channel and also for a p -doped channel (see Appendices I and J).

To elucidate the evolution of the conductance steps with magnetic field, we simulate the experimental setup using two independent, complementary theoretical approaches, $k \cdot p$ theory [23] and tight-binding calculations [25] (see the supplement for technical details). Both approaches agree well with each other and the experiment, highlighting the robustness of the observed features and the validity of our two modelling approaches. They reproduce and explain the observed low-field splitting (Fig. 3) and the level crossing pattern (Fig. 4).

Here, we use soft electrostatic confinement provided by a transverse electric field both at $B = 0$ and at a finite magnetic field. The obtained magnetic field dependence of the miniband edges represents the closest spectral analogue of the experimentally measured transconductance spectrum. We chose the potential landscape for $k \cdot p$ theory by matching the mode spacing extracted from finite bias measurements of QPC M at $B = 0$ T (see Appendix K). Note that in the experiment the channel gate voltage influences not only the Fermi level, but also the shape of the confinement potential and the size of the displacement field inside the channel. To obtain one to one agreement between the calculation and the experimental results, a self-consistent potential would be required.

At zero magnetic field, we find spin- and valley-degenerate spectra (Fig. 3a) in agreement with the experimentally observed step size of $\Delta G = 4 e^2/h$ (Fig. 2a). The subband edges (for small mode numbers) are situated at finite momenta, reminiscent of the three mini-valleys in gapped BLG in the presence of trigonal warping [23, 26]. When switching on a magnetic field, the interlayer asymmetry leads to valley splitting of electron subbands, clearly seen in the band structure computed

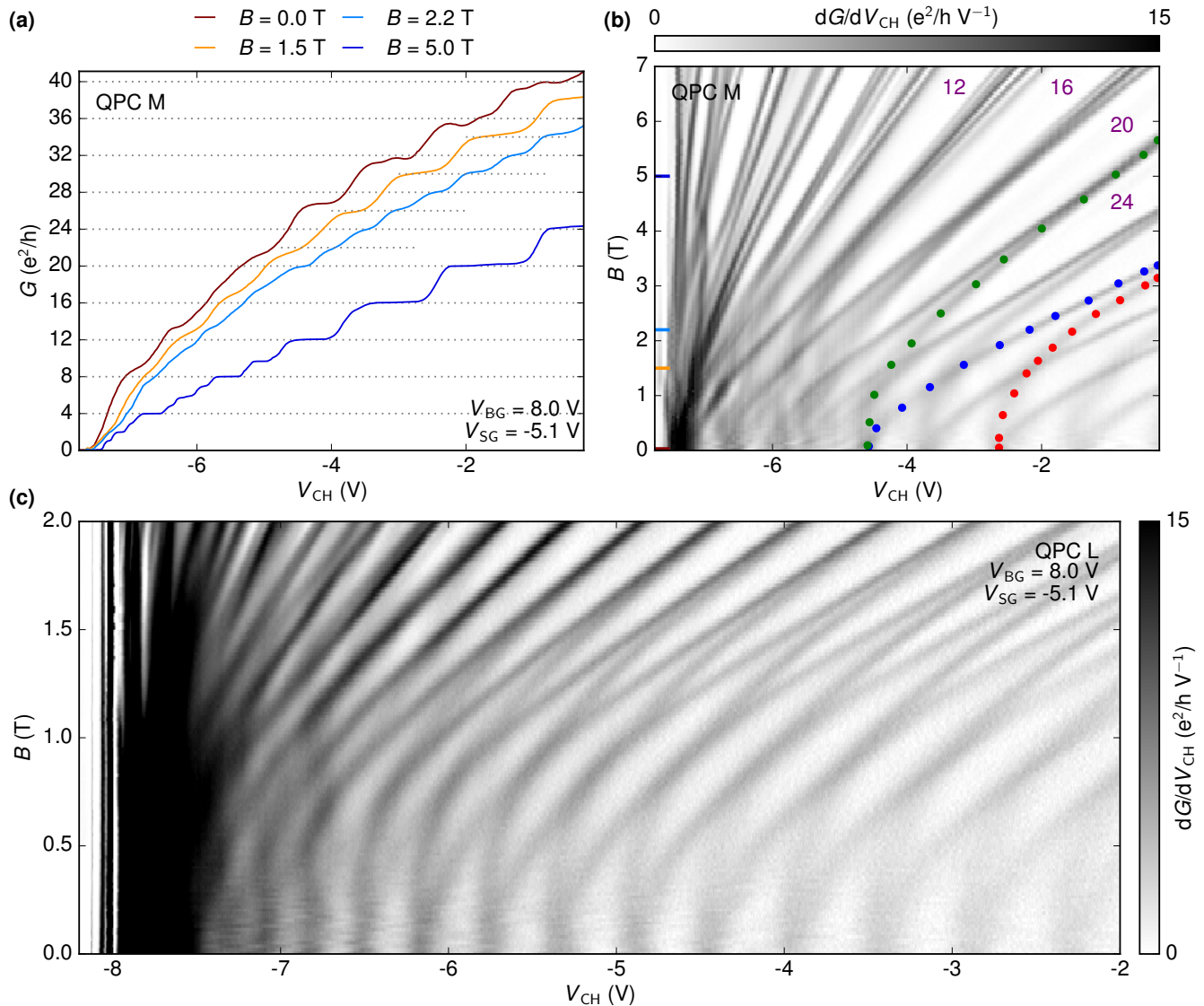


FIG. 2. (a) Conductance of QPC M as a function of V_{CH} for various magnetic field strengths. Several quantization sequences are observed. (b) Transconductance of QPC M as a function V_{CH} and magnetic field. A pattern of mode splittings (see green and blue dotted modes) is observed. Numbers in purple indicate the conductance values in the quantum Hall regime. (c) Transconductance of QPC L as a function V_{CH} and magnetic field. A similar pattern of mode crossings is observed in a smaller magnetic field range than for QPC M.

for $B = 2.2$ T (Fig. 3b, blue and magenta subbands). This lifting of valley degeneracy is in agreement with the measured step size of $\Delta G = 2 e^2/h$ (see Fig. 2a). The linearity of the valley splitting of the subband edges with B , Fig. 3b, is related to the fact that the zero-field states $|n_\xi\rangle$ (with transverse quantum number $n = 0, 1, \dots$ in the K_ξ ($\xi = \pm$) valley) of trigonally warped gapped BLG [23, 26] carry non-trivial Berry curvature (see insets of Fig. 3 and in Appendix B) and, consequently, a finite magnetic moment, M_z . For larger displacement fields, the Berry curvature becomes more spread out in k -space around the K -points, affecting several of the lowest modes.

In the high magnetic field regime, where the magnetic

length is smaller than the channel width, the subbands in the channel become drifting states in the BLG Landau levels (LLs) $|N_\xi\rangle$, where N now indicates the LL index. The LL spectrum of BLG has a pair of special states $N = 0, 1$, that appear at zero energy in ungapped BLG with the wave functions residing on different layers in the opposite valleys. After the displacement field introduces a layer asymmetry gap, these states split apart by Δ , resulting in the two lowest conduction band subbands belonging to only one valley, e.g. K_+ (then, the highest valence band subbands would be from valley K_-). The other LLs in both valleys with $N \geq 2$ have approximately the same weight on the sublattices in the two layers and

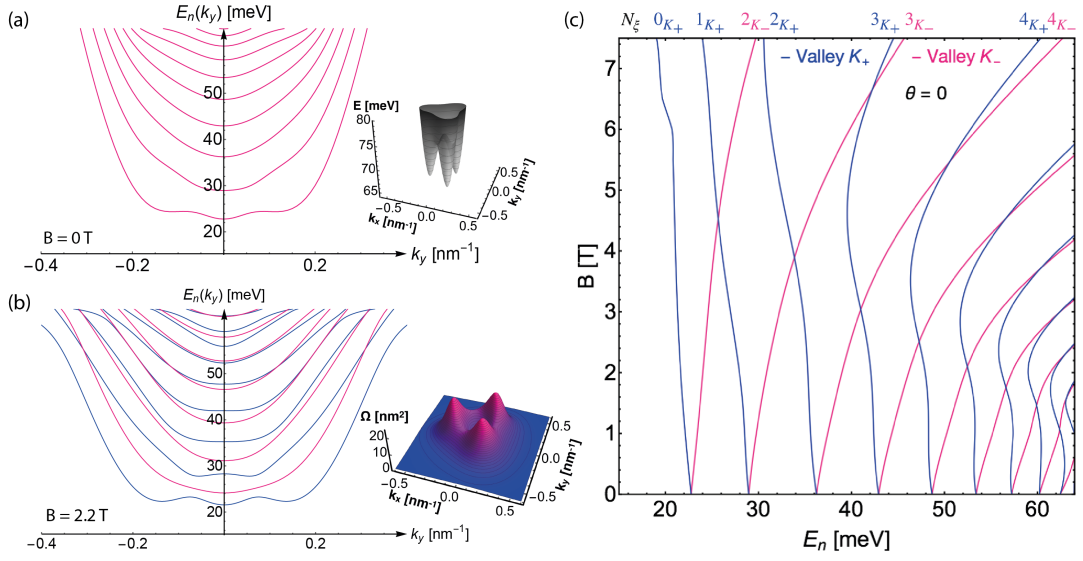


FIG. 3. (a) Bandstructure (conduction band) at $B = 0$ T of BLG in the presence of a confinement potential $U(x)$ and a modulated gap $\Delta(x)$ as described in the text showing a discrete, valley degenerate mode spectrum. Inset: lowest conduction band of homogeneous gapped BLG (K_- valley) for $\Delta_0 = 150$ meV with three minivalleys forming around the K -point. (b) Bandstructure (conduction band) of the channel at $B = 2.2$ T, where symmetry between valleys is broken. The valley splitting at small magnetic fields is proportional to the magnetic field. Inset: Berry curvature Ω of the corresponding states with non-zero peaks in the three minivalleys. (c) Magnetic field dependence of the subband edges of the conduction bands in the electron channel. The nontrivial Berry curvature of the zero-field states implies a non-zero orbital magnetic moment M of the states, $M \propto \Omega$, which induces the linear in magnetic field splitting at small magnetic fields. At high magnetic fields the levels evolve into the LLs of gapped BLG.

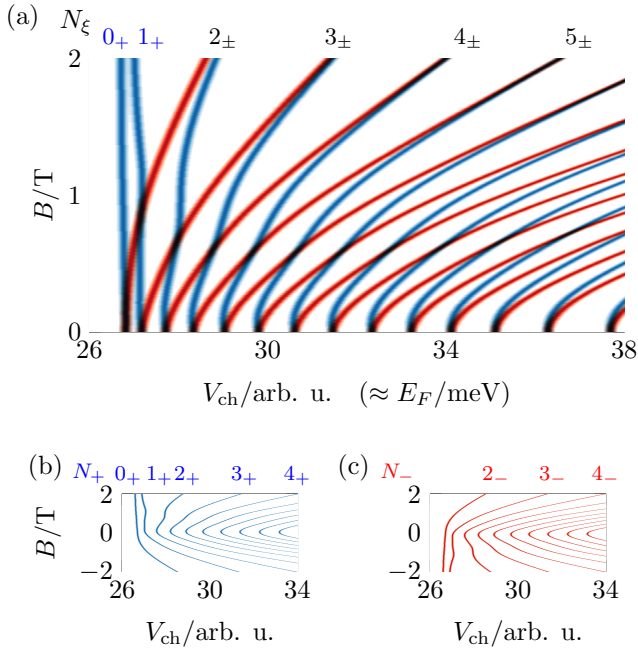


FIG. 4. a) Differential conductance dG/dE of a 180 nm wide BLG nanoribbon, including a thermal smoothing of 1.7 K. b) and c) show separately the contributions from the two valleys K_+ and K_- at low energies. The channel voltage is determined through the relation $V_{ch} \propto \sqrt{E_F^2 - (\Delta/2)^2}$, with $\Delta/2 = 25$ meV.

very close energies. Such an asymptotic behavior corresponds to the evolution of the subbands such that subbands $(n+2)_{K_+}$ eventually merge with subbands n_{K_-} upon an increase in magnetic field as shown in Fig. 4a. For $B < 0$, the same pattern emerges with the two valleys interchanged (see Fig. 4b,c).

Note that the absence of hard edges characteristic for the present electrostatically defined bilayer constriction is critical for observing the interweaving pattern of crossing states. In rough-edged constrictions broken valley symmetry due to scattering quickly obscure the underlying pattern. These difficulties aside, a similar crossing pattern appears in principle in single layer graphene, as we have verified numerically for an ideal constriction (see Appendix G).

In conclusion, we reported on the experimental observation of the mode crossing pattern during the evolution from size quantization to the Hall regime in BLG QPC. A valley splitting linear in magnetic field could be explained by a non-trivial orbital magnetic moment of states in gapped BLG. Our experimental results could be reproduced by numerical simulations.

ACKNOWLEDGEMENTS

We thank A. Rebhan for fruitful discussions. We acknowledge financial support from the European Graphene Flagship, the Swiss National Science Foun-

ation via NCCR Quantum Science and Technology, ERC Synergy Hetero 2D, WWTF project MA14-002 and MECD. Calculations were performed on the Vienna Scientific Cluster (VSC). Growth of hexagonal boron nitride crystals was supported by the Elemental Strategy Initiative conducted by MEXT, Japan and the CREST (JP-MJCR15F3), JST.

-
- [1] B J Van Wees and H Van Houten, “Quantized conductance of point contacts in a two-dimensional electron gas,” *Physical Review Letters* **60**, 848–850 (1988).
- [2] D A Wharam, T J Thornton, R Newbury, M Pepper, H Ahmed, J E F Frost, D G Hasko, D C Peacock, D A Ritchie, and G A C Jones, “One-dimensional transport and the quantisation of the ballistic resistance,” *Journal of Physics C: Solid State Physics* **21**, L209–L214 (1988).
- [3] L. P. Rokhinson, L. N. Pfeiffer, and K. W. West, “Spontaneous spin polarization in quantum point contacts,” *Physical Review Letters* **96**, 156602 (2006).
- [4] R. Danneau, W. R. Clarke, O. Klochan, A. P. Micolich, A. R. Hamilton, M. Y. Simmons, M. Pepper, and D. A. Ritchie, “Conductance quantization and the $0.7 \times 2e^2/h$ conductance anomaly in one-dimensional hole systems,” *Applied Physics Letters* **88** (2006), 10.1063/1.2161814.
- [5] D Többen, D A Wharam, G Abstreiter, J P Kotthaus, and F Schäffler, “Ballistic electron transport through a quantum point contact defined in a $\{Si/Si_{0.7}Ge_{0.3}\}$ heterostructure,” *Semicond. Sci. Technol.* **10**, 711–714 (1995).
- [6] H. T. Chou, S. Lüscher, D. Goldhaber-Gordon, M. J. Manfra, A. M. Sergent, K. W. West, and R. J. Molnar, “High-quality quantum point contacts in GaN/AlGaIn heterostructures,” *Applied Physics Letters* **86**, 1–3 (2005).
- [7] N. Goel, J. Graham, J. C. Keay, K. Suzuki, S. Miyashita, M. B. Santos, and Y. Hirayama, “Ballistic transport in InSb mesoscopic structures,” *Physica E: Low-Dimensional Systems and Nanostructures* **26**, 455–459 (2005).
- [8] O. Gunawan, B. Habib, E. P. De Poortere, and M. Shayegan, “Quantized conductance in an AlAs two-dimensional electron system quantum point contact,” *Physical Review B* **74**, 155436 (2006).
- [9] R. Mizokuchi, R. Maurand, F. Vigneau, M. Myronov, and S. De Franceschi, “Ballistic one-dimensional holes with strong g-factor anisotropy in germanium,” *Phys. Rev. Lett.* **121**, 1–23 (2018).
- [10] Nikolaos Tombros, Alina Veligura, Juliane Junesch, Marcos H. D. Guimarães, Ivan J. Vera Marun, Harry T. Jonkman, and Bart J. van Wees, “Quantized conductance of a suspended graphene nanoconstriction,” *Nature Physics* **7**, 697–700 (2011).
- [11] B. Terrés, L. A. Chizhova, F. Libisch, J. Peiro, D. Jörges, S. Engels, A. Girschik, K. Watanabe, T. Taniguchi, S. V. Rotkin, J. Burgdörfer, and C. Stampfer, “Size quantization of Dirac fermions in graphene constrictions,” *Nature Communications* **7**, 1–7 (2016).
- [12] Minsoo Kim, Ji-Hae Choi, Seung-Hoon Lee, Kenji Watanabe, Takashi Taniguchi, Sang-Hoon Jhi, and Hui-Jong Lee, “Valley-symmetry-preserved transport in ballistic graphene with gate-defined carrier guiding,” *Nature Physics* (2016), 10.1038/nphys3804.
- [13] M T Allen, J Martin, and A Yacoby, “Gate-defined quantum confinement in suspended bilayer graphene,” *Nature Communications* **3**, 934 (2012).
- [14] Augustinus Stijn M Goossens, Stefanie C M Driessen, Tim A Baart, Kenji Watanabe, Takashi Taniguchi, and Lieven M K Vandersypen, “Gate-defined confinement in bilayer graphene-hexagonal boron nitride hybrid devices,” *Nano Letters* **12**, 4656–60 (2012).
- [15] Hiske Overweg, Hannah Eggimann, Xi Chen, Sergey Slizovskiy, Marius Eich, Pauline Simonet, Riccardo Pisoni, Yongjin Lee, Kenji Watanabe, Takashi Taniguchi, Vladimir Fal’ko, Klaus Ensslin, and Thomas Ihn, “Electrostatically induced quantum point contact in bilayer graphene,” *Nano Letters* **18**, 553–559 (2018).
- [16] A. N. Redlich, “Parity violation and gauge noninvariance of the effective gauge field action in three dimensions,” *Physical Review D* **29**, 2366–2374 (1984).
- [17] Mengqiao Sui, Guorui Chen, Liguang Ma, Wen Yu Shan, Dai Tian, Kenji Watanabe, Takashi Taniguchi, Xiaofeng Jin, Wang Yao, Di Xiao, and Yuanbo Zhang, “Gate-tunable topological valley transport in bilayer graphene,” *Nature Physics* **11**, 1027–1031 (2015), arXiv:1501.04685.
- [18] A. Cortijo, F. Guinea, and M. A.H. Vozmediano, “Geometrical and topological aspects of graphene and related materials,” *Journal of Physics A: Mathematical and Theoretical* **45** (2012), 10.1088/1751-8113/45/38/383001, arXiv:1112.2054.
- [19] K. S. Novoselov, E. McCann, S. V. Morozov, V. I. Fal’ko, M. I. Katsnelson, U. Zeitler, D. Jiang, F. Schedin, and A. K. Geim, “Unconventional quantum Hall effect and Berry’s phase of 2π in bilayer graphene,” *Nature Physics* **2**, 177–180 (2006), arXiv:0602565 [cond-mat].
- [20] C.N.R. Rao and A.K. Sood, *Graphene: Synthesis, Properties, and Phenomena* (Wiley, 2013).
- [21] T. Taychatanapat, K. Watanabe, T. Taniguchi, and P. Jarillo-Herrero, “Quantum hall effect and Landau-level crossing of Dirac fermions in trilayer graphene,” *Nature Physics* **7**, 621–625 (2011).
- [22] L Wang, I Meric, P Y Huang, Q Gao, Y Gao, H Tran, T Taniguchi, K Watanabe, L M Campos, D a Muller, J Guo, P Kim, J Hone, K L Shepard, and C R Dean, “One-dimensional electrical contact to a two-dimensional material,” *Science* **342**, 614–7 (2013).
- [23] Edward McCann and Vladimir I. Fal’ko, “Landau-level degeneracy and quantum hall effect in a graphite bilayer,” *Physical Review Letters* **96**, 086805 (2006), arXiv:0510237 [cond-mat].
- [24] A. Knothe and V. Fal’ko, “How do minivalleys and Berry curvature influence electrostatically induced conduction channels in gapped bilayer graphene?” (2018).

- [25] F. Libisch, S. Rotter, and J. Burgdörfer, “Coherent transport through graphene nanoribbons in the presence of edge disorder,” *New Journal of Physics* **14**, 123006 (2012).
- [26] Anastasia Varlet, Dominik Bischoff, Pauline Simonet, Kenji Watanabe, Takashi Taniguchi, Thomas Ihn, Klaus Ensslin, Marcin Mucha-Kruczyński, and Vladimir I. Fal’ko, “Anomalous Sequence of Quantum Hall Liquids Revealing a Tunable Lifshitz Transition in Bilayer Graphene,” *Physical Review Letters* **113**, 116602 (2014).
- [27] Di Xiao, Ming Che Chang, and Qian Niu, “Berry phase effects on electronic properties,” *Reviews of Modern Physics* **82**, 1959–2007 (2010), arXiv:0907.2021.
- [28] Ming Che Chang and Qian Niu, “Berry phase, hyper-orbits, and the Hofstadter spectrum,” *Physical Review Letters* **75**, 1348–1351 (1995), arXiv:9511014 [cond-mat].
- [29] Jeil Jung and Allan H. MacDonald, “Accurate tight-binding models for the π bands of bilayer graphene,” *Physical Review B - Condensed Matter and Materials Physics* **89**, 035405 (2014).
- [30] S. Sanvito, C.J. Lambert, J.H. Jefferson, and A.M. Bratkovsky, “General green’s-function formalism for transport calculations with spd hamiltonians and giant magnetoresistance in co- and ni-based magnetic multilayers,” *Phys. Rev. B* **59**, 11936–11948 (1999).

Appendix A: Model Hamiltonian

The four-band model Hamiltonian of BLG (BLG) is given by [23, 26]

$$H_{BLG}^{\xi} = \xi \begin{pmatrix} \xi U(x) - \frac{1}{2}\Delta(x) & v_3\pi & 0 & v\pi^{\dagger} \\ v_3\pi^{\dagger} & \xi U(x) + \frac{1}{2}\Delta(x) & v\pi & 0 \\ 0 & v\pi^{\dagger} & \xi U(x) + \frac{1}{2}\Delta(x) & \xi\gamma_1 \\ v\pi & 0 & \xi\gamma_1 & \xi U(x) - \frac{1}{2}\Delta(x) \end{pmatrix}, \quad (\text{A1})$$

written in the basis $\Phi_{K^+} = (\Psi_{A1}, \Psi_{B2}, \Psi_{A2}, \Psi_{B1})$ or $\Phi_{K^-} = (\Psi_{B2}, \Psi_{A1}, \Psi_{B1}, \Psi_{A2})$ in the two valleys K^+ (for $\xi = +1$), and K^- (for $\xi = -1$). The diagonal terms in this Hamiltonian account for the spatially modulated confinement potential $U(x)$ and the modulated gap $\Delta(x)$:

$$U(x) = \frac{U_0}{\cosh \frac{x}{L}}, \quad \Delta(x) = \Delta_0 - \beta \frac{\Delta_0}{\cosh \frac{x}{L}}, \quad (\text{A2})$$

where we chose $U_0 = -30$ meV, $L = 20$ nm, and $\beta = 0.3$, in accordance with the parameters of the experimental probes. Furthermore, $\pi = p_x + ip_y$, $\pi^{\dagger} = p_x - ip_y$, with $\mathbf{p} = -i\hbar\nabla - \frac{e}{c}\mathbf{A}$ and for the velocities and hoppings we use $v = 1.0228 * 10^6$ m/s, $v_3 = 1.2299 * 10^5$ m/s, and $\gamma_1 = 381$ meV [26].

Appendix B: Bulk properties

In the limit $x \rightarrow \infty$ the Hamiltonian of Eq. A1 describes the properties of homogeneous gapped BLG. The dispersion is given by the four valley degenerate bands [23]

$$E_{\pm}^{\alpha} = \pm \frac{\gamma_1^2}{2} + \frac{\Delta^2}{4} + (v^2 + \frac{v_3^2}{2})\hbar^2 k^2 + (-1)^{\alpha} \left(\frac{(\gamma_1^2 - v_3^2 \hbar^2 k^2)^2}{4} + v^2 \hbar^2 k^2 [\gamma_1^2 + \Delta^2 + v_3^2 \hbar^2 k^2] + 2\xi\gamma_1 v_3 v^2 \hbar^3 k^3 \cos 3\varphi \right)^{\frac{1}{2}}, \quad (\text{B1})$$

where $\alpha = 1, 2$, and $\mathbf{k} = k(\cos \varphi, \sin \varphi)$. In the top panel of Fig. 5 we plot the lower conduction band ($\alpha = 1$) in the K_- valley for a gap of $\Delta_0 = 150$ meV demonstrating the effect of trigonal warping induced by $v_3 \neq 0$ causing the dispersion to form three mini-valleys around each K -point. The states of gapped BLG carry a non-trivial Berry curvature and orbital magnetic moment. From the Bloch functions of the n th band the magnitude of the corresponding Berry curvature $\Omega_n(\mathbf{k}) = \Omega_n \mathbf{e}_z$ and the orbital magnetic moment $\mathbf{M}_n(\mathbf{k}) = M_n \mathbf{e}_z$ can be computed according to Refs. [27, 28]

$$\Omega_n(\mathbf{k}) = i \langle \nabla_{\mathbf{k}} \Phi_n | \times | \nabla_{\mathbf{k}} \Phi_n \rangle \mathbf{e}_z, \\ M_n(\mathbf{k}) = -i \frac{e}{\hbar} \langle \nabla_{\mathbf{k}} \Phi_n | \times [\epsilon_n(\mathbf{k}) - H(\mathbf{k})] | \nabla_{\mathbf{k}} \Phi_n \rangle \mathbf{e}_z,$$

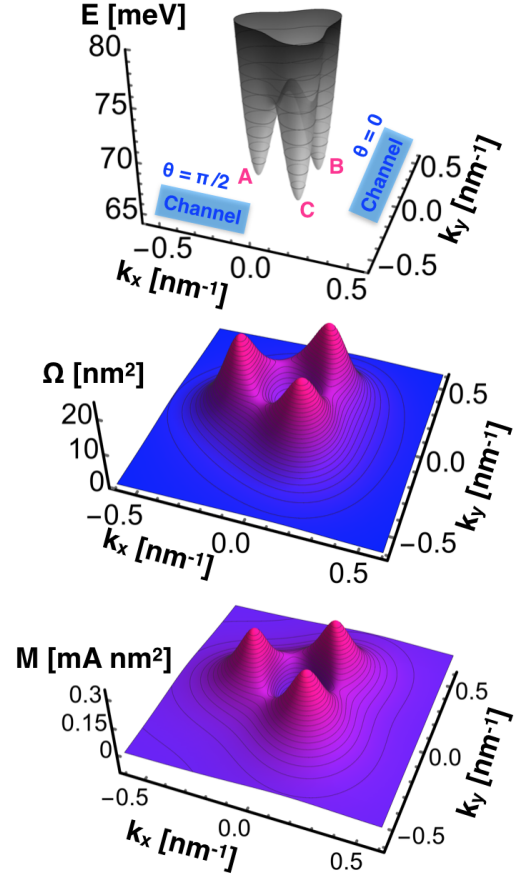


FIG. 5. Top: Dispersion of homogeneous, gapped BLG in the K_- valley (lower conduction band for $\Delta = 150$ meV). The letters A, B, and C label the three anisotropic minivalleys that form around each K -point due to trigonal warping. The blue stripes indicate the orientation of the channel at angles $\theta = 0$ or $\theta = \pi/2$, respectively. Bottom: Corresponding Berry curvature Ω and magnetic moment M of the states of the lower conduction band in the K_- valley for $\Delta = 150$ meV. In the K_+ valley the sign of both Ω and M is reversed.

where $\nabla_{\mathbf{k}} = (\partial_{k_x}, \partial_{k_y})$ and " \times " denotes the two-dimensional cross product. We plot the Berry curvature and the magnetic moment of the lower conduction band in the K_- -valley in the lower panels of Fig. 5 for $\Delta = 150$ meV. In the K_+ -valley both Ω and M carry the opposite sign. A non-zero orbital magnetic momentum behaves like the electron spin [27] and will hence couple linearly to a magnetic field through a Zeeman-like term $-\mathbf{M}(\mathbf{k}) \cdot \mathbf{B}$.

Appendix C: Numerical diagonalization inside the channel

In the presence of a nontrivial confinement potential we diagonalize the Hamiltonian in Eq. A1 numerically in a basis of harmonic oscillator wave functions

$\psi_n(x) = N_n e^{-\frac{1}{2}(\alpha x)^2} \mathcal{H}_n(\alpha x)$, where $N_n = \sqrt{\frac{\alpha}{\sqrt{\pi} 2^n n!}}$ is the normalization constant and α is a scaling factor of unit length^{-1} ; we choose α adapted to the potential $U(x)$ obtained from comparing a parabolic potential to $U(x)$. We assume free propagation of the electrons in the y -direction. The basis states are then of the form $\Psi_n(\mathbf{r}) = e^{ik_y y} \Phi_n(x)$ where the x -dependent part is given by

$$\Phi_{n,1}(x) = \begin{pmatrix} \psi_n(x) \\ 0 \\ 0 \\ 0 \end{pmatrix}, \quad \Phi_{n,2} = \begin{pmatrix} 0 \\ \psi_n(x) \\ 0 \\ 0 \end{pmatrix},$$

$$\Phi_{n,3} = \begin{pmatrix} 0 \\ 0 \\ \psi_n(x) \\ 0 \end{pmatrix}, \quad \Phi_{n,4} = \begin{pmatrix} 0 \\ 0 \\ 0 \\ \psi_n(x) \end{pmatrix}. \quad (\text{C1})$$

For every set of system parameters we construct the matrix corresponding to Hamiltonian H_{BLG}^ξ in the basis given in Eq. C1 and obtain the energy spectrum by diagonalization. Convergence is reached when the energy levels do not change anymore upon including a higher

number of basis states. In order to include a magnetic field we do Peierls substitution in the Hamiltonian in Eq. A1 : $\pi \rightarrow \pi - \frac{e}{c} \mathbf{A}$. For a magnetic field perpendicular to the BLG sheet and to preserve translational invariance in the y -direction we chose Landau gauge of the form $\mathbf{A} = (0, -Bx, 0)$. The basis states of Eq. C1 then translate into the basis of Landau level wave functions localized at Landau orbital $x_0 = 0$.

Appendix D: Channel spectra for different parameters

Due to the trigonal warping effect for non-zero v_3 the dispersion is not rotationally symmetric (*c.f.* the dispersion of homogeneous gapped BLG in Fig. 5) and the channel spectra therefore depend on the orientation of the channel. We distinguish between the two angles of orientation $\theta = 0$ and $\theta = \frac{\pi}{2}$ for which the orientation of the channel is indicated by the blue bars in Fig. 5. In Fig. 6 we show additional channel spectra for different system parameters and the two different angles of orientation. Figure 7 shows the dependence of the lower band edges as a function of the magnetic field for both angles.

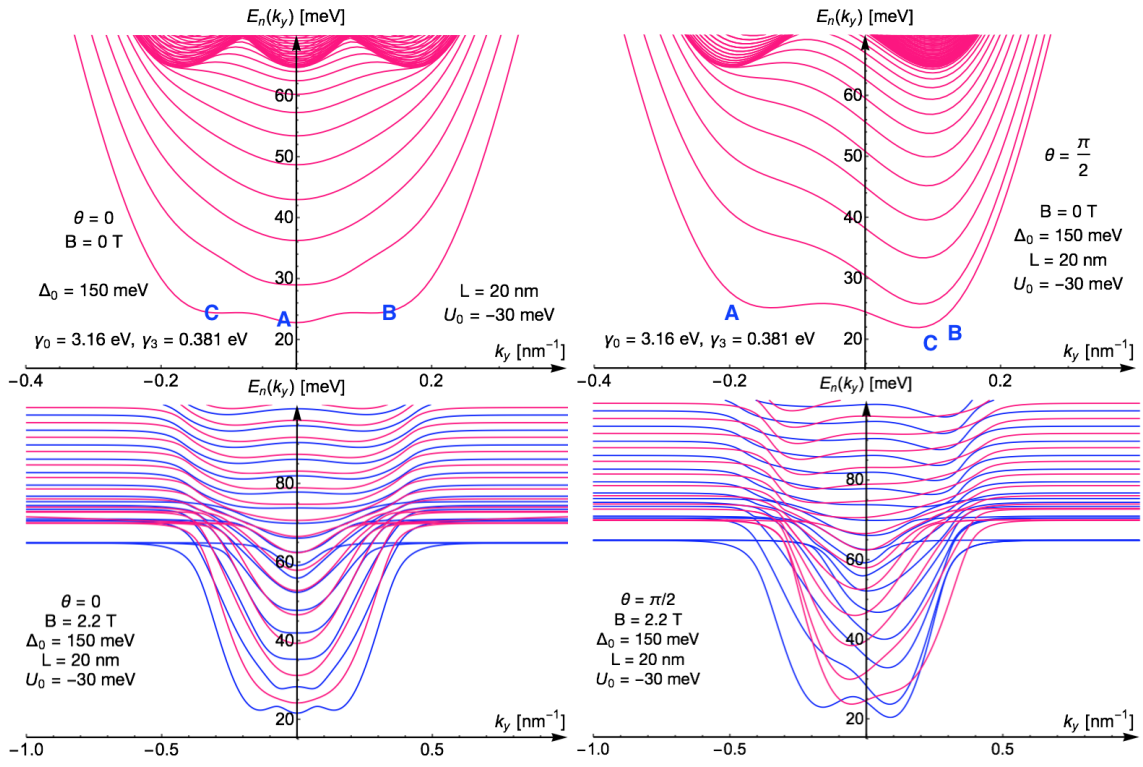


FIG. 6. Conduction band spectra inside the channel for the two different orientations $\theta = 0$ and $\theta = \frac{\pi}{2}$. Top: Spectra in the absence of a magnetic field. The letters A , B , and C refer to the minivalleys indicated in Fig. 5. Bottom: Magnetic spectra for a magnetic field of $B = 2.2$ T. In the presence of a non-trivial gap and a non-zero magnetic field valley symmetry is broken and we obtain two unrelated spectra for the K_+ valley (blue lines) and the K_- valley (magenta lines), where the splitting between valleys is given by the Zeeman splitting of magnetic moment-carrying states in the minivalleys of gapped BLG.

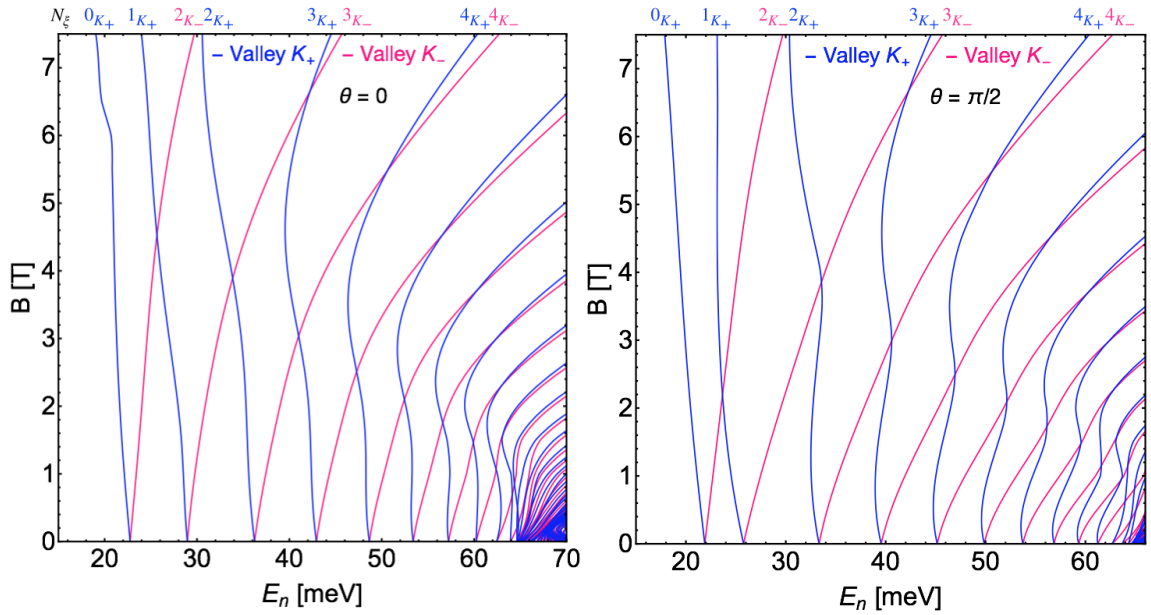


FIG. 7. Conduction band edges as a function of the magnetic field strength for the same system parameters as indicated in Fig. 6 and the two different channel orientations $\theta = 0$ and $\theta = \frac{\pi}{2}$. We observe linear behaviour of the levels at low magnetic field due to the linear Zeeman coupling induced by the magnetic moment (due to the finite Berry curvature) of the states in the minivalleys of gapped BLG. At high magnetic fields, the levels evolve into the LLs of gapped BLG.

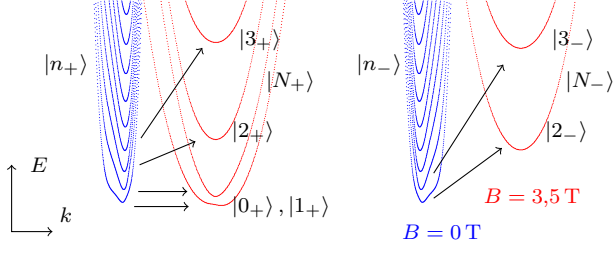


FIG. 8. Bandstructure at $B = 0$ T (blue) featuring size quantized energy levels $|n_\xi^S\rangle$ and Landau states $|n_\xi^L\rangle$ at $B = 3.5$ T (red) $|n_\xi^S\rangle$. Two zero modes form (for $B > 0$) only in the K_+ valley. The analytical form of the states is given in Eq. F2

Appendix E: Details of the tight binding simulation

Our tight binding calculation is done for a 280 nm wide BLG nanoribbon in the parametrisation given by Jung et al. [29]. An additional displacement field, which we obtain from solving the Poisson equation for the experimental setup QPC L at constant channel voltage $V_{\text{ch}} = -2.5$ V, is added. It confines the wavefunctions to the 180 nm wide region between the gates, where the displacement field is about 50 meV. A Berry-Mondragon type potential at the sides of the ribbon is used to eliminate edge states, restricting the simulation effectively to a width of 250 nm. We then solve the eigenvalue problem for the Bloch state [30]

$$\left(\mathcal{H}_0 + e^{ik\Delta x}\mathcal{H}_I + e^{-ik\Delta x}\mathcal{H}_I^\dagger\right)\chi = E\chi, \quad (\text{E1})$$

for a given k numerically, which has wavefunctions $\psi = \chi \exp(ik\Delta x)$ of an infinite waveguide as solutions. The bandstructure is given by the eigenvalues $E(k)$, see Fig. 8. The matrix \mathcal{H}_0 contains all on-site energies and hopping matrix elements of a slice in y direction, and the matrix \mathcal{H}_I contains the hopping matrix elements between a given slice and the one to the right, separated by Δx . As direction of propagation we choose an angle $\phi = \arctan(1/(2\sqrt{3})) \approx 0.28$ rad away from armchair direction. In armchair direction, the two cones lie on top of each other in momentum space, making a clean separation of K_+ and K_- states challenging.

Appendix F: Effective low-energy Hamiltonian

The minimal ingredients which lead to the observed crossing pattern are already present in the effective low-energy Hamiltonian of BLG. For completeness, we present a short discussion.

We consider Bernal-stacked BLG, with A and B atoms in the lower layer, and A' (coupled to B) and B' atoms in the upper layer. Eliminating the dimer state components leads to an effective low-energy Hamiltonian written in

terms of the wavefunction on the unpaired (A and B') atoms, A magnetic field $\mathbf{B} = (0, 0, B)$, $B > 0$, can be added with the minimal coupling prescription $\hat{\mathbf{p}} \rightarrow \hat{\mathbf{p}} - q\mathbf{A}/c$. With the confinement in y direction in mind, we choose the gauge $\mathbf{A} = (-By, 0, 0)$. The Hamiltonian then reads

$$\mathcal{H}_{2,\xi} = -\frac{1}{2m\lambda_B^2} \left((\xi\tilde{y} + ip_{\tilde{y}})^2 \right) \quad (\text{F1})$$

where we define the magnetic length $\lambda_B = \sqrt{\hbar c/(eB)}$ and $\tilde{y} = y/\lambda_B + \lambda_B k_x$, $m = \gamma_1/(2v^2)$, interlayer coupling γ , Fermi velocity v , valley index $\xi = \pm 1$. It has the solutions [23] for K_+ and $n \geq 2$

$$E_{n,\pm} = \pm\hbar\omega_c\sqrt{n(n-1)}, \quad |n_{K_+}^L\rangle_\pm = \frac{1}{\sqrt{2}} \begin{pmatrix} \phi_n \\ \pm\phi_{n-2} \end{pmatrix}. \quad (\text{F2})$$

$\omega_c = 1/(m\lambda_B^2)$ and two zero-energy solutions

$$E = 0 \quad |(n=0, 1)_{K_+}^L\rangle_\pm = \begin{pmatrix} \phi_n \\ 0 \end{pmatrix}. \quad (\text{F3})$$

The localization of the lowest lying Landau on a single sublattice results – due to the absence of nearest neighbors – in zero-energy solutions of the effective Hamiltonian. Near K_- we find the same spectrum but with the A and B' sublattices reversed.

a. Magnetic Field and displacement field A displacement field $\sigma^z\Delta/2$ acts as an effective mass term and lifts the K_ξ degeneracy[23],

$$E_{n,\pm} = \pm\hbar\omega_c\sqrt{n(n-1)} - \xi\frac{\Delta}{2}\frac{\hbar\omega_c}{\gamma_1}, \quad n \geq 2. \quad (\text{F4})$$

The two zero modes are shifted above (K_+) or below (K_-) the gap[23],

$$E_0 = \xi\frac{\Delta}{2}, \quad E_1 = \xi\frac{\Delta}{2} - \xi\frac{\Delta\omega_c}{\gamma_1}. \quad (\text{F5})$$

The states which are localized on one sublattice and thus localized on one of the layers are trivially affected by the electrostatic potential: The zeroth Landau levels where ξB is positive gets shifted above the gap, and the level where ξB is negative is shifted below the gap.

Appendix G: Monolayer Graphene

A similar effect can be observed in monolayer graphene, see Fig. 9.

The only difference is that due to the existence of a single zero mode instead of two in the quantum Hall regime, the evolution now follows the pattern $|(n-1)_-^S\rangle \rightarrow |n_-^L\rangle$ and $|n_+^S\rangle \rightarrow |n_+^L\rangle$ for positive B , and with the roles of K_+ and K_- reversed for negative B .

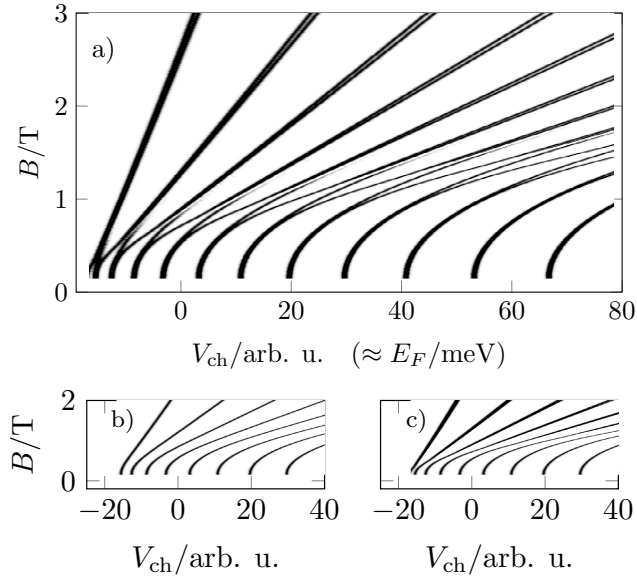


FIG. 9. a) Differential conductance dG/dE in a 280 nm wide monolayer graphene ribbon, including a thermal smoothening of 1.7 K. A potential confines the states to a region of 180 nm. A Berry-Mondragon type potential at the sides of the ribbon is used to eliminate edge states. b) and c) show separately the contributions from the two valleys K_+ and K_- at low energies.

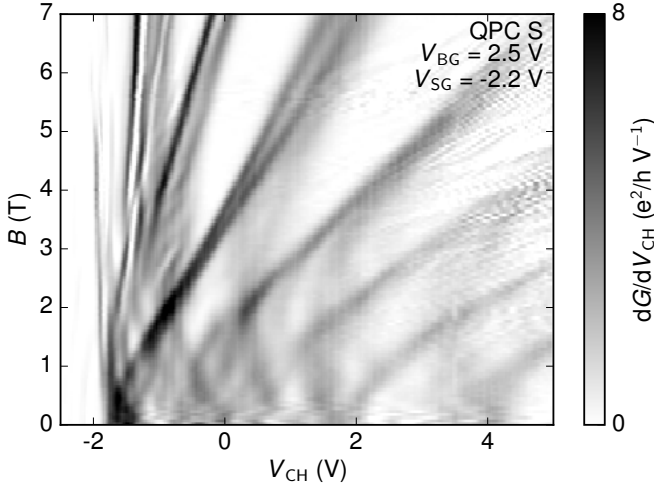


FIG. 10. Transconductance of QPC S as a function of channel gate voltage and magnetic field. Several mode crossings can be observed. The spacing between the modes is larger than for QPC M and QPC L, as expected for a narrower channel.

Appendix H: Transconductance of QPC S

The transconductance of QPC S as a function of channel gate voltage and magnetic field is shown in Fig. 10. It shows a pattern of mode crossings similar to the patterns of QPC M and QPC L (see Fig. 2b,c), with a larger mode spacing due to the narrower confinement potential.

Appendix I: Transconductance in a lower displacement field

Figure 11 shows the transconductance of QPC M as a function of channel gate voltage and magnetic field for $V_{BG} = 2.5 V$ and $V_{SG} = -2.2 V$. Although this corresponds to a smaller displacement field in the channel than in Fig. 2b, a similar pattern of mode crossings is observed. No modes can be observed in the top right corner of Fig. 11, because in this regime the filling factor in the bulk is smaller than the filling factor in the channel.

Appendix J: Transconductance in the p -type regime

The pattern of mode crossing can also be observed for a p -type channel, as shown for QPC M in Fig. 12.

Appendix K: Finite bias diamonds

Figure 13 shows the finite bias measurements of the modes of QPC L, showing a mode spacing on the order of 3 meV at $B = 0.5 T$. From the slope of the diamond boundaries (see red dashed line in Fig. 13), a lever arm

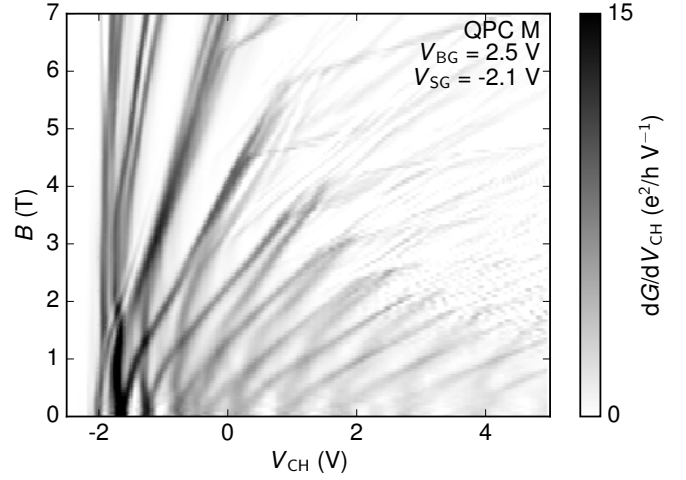


FIG. 11. Transconductance of QPC M as a function of channel gate voltage and magnetic field for $V_{BG} = 2.5 V$. The observed pattern of mode crossings is similar to the pattern in Fig. 2b.

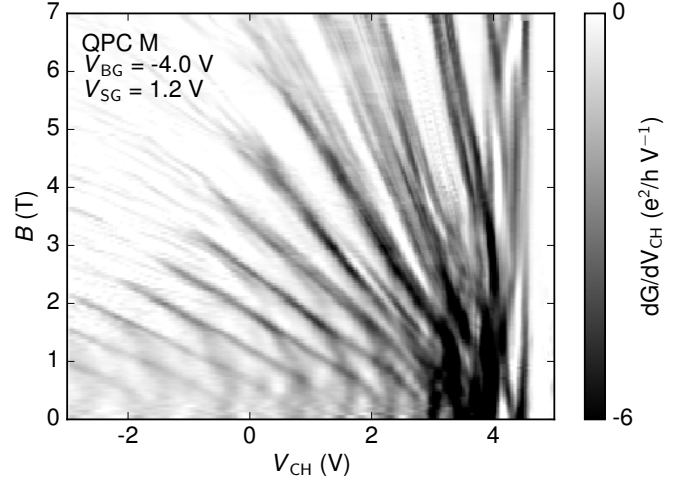


FIG. 12. Transconductance of QPC M as a function of channel gate voltage and magnetic field for a p -type channel. For the higher modes (at $V_{CH} < 2 V$) the pattern of mode crossings looks similar to that observed in Fig. 2b.

α for conversion from channel gate voltage to energy can be extracted ($E = \alpha e V_{CH}$). For QPC L we find $\alpha = 18 \times 10^{-3}$ and for QPC M we find $\alpha = 14 \times 10^{-3}$. The smaller lever arm for the narrower QPC is due to more significant screening of the channel gate voltage for this QPC.

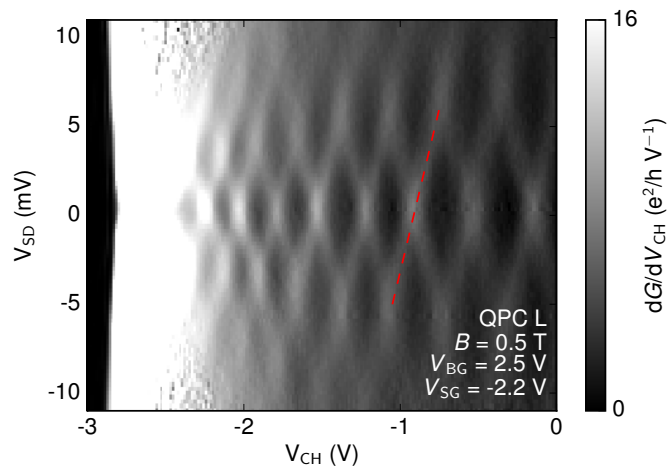


FIG. 13. Finite bias spectroscopy of QPC L. A typical diamond pattern is observed. From the slope of finite bias diamond boundaries, the lever arm of the channel gate can be determined.